Durham University

Durham Research Online

Deposited in DRO:

06 November 2020

Version of attached file:

Accepted Version

Peer-review status of attached file:

Peer-reviewed

Citation for published item:

Naseer, Amtul and Hussain, Murid and Shakir, Imran and Abbas, Qaisar and Yilmaz, Duygu and Zahra, Marriam and Raza, Rizwan (2020) 'The robust catalysts (Ni1–Mo /doped ceria and Zn1–Mo /doped ceria, x=0.1 and 0.3) for efficient natural gas reforming in solid oxide fuel cells.', Electrochimica Acta., 361 . p. 137033.

Further information on publisher's website:

https://doi.org/10.1016/j.electacta.2020.137033

Publisher's copyright statement:

© 2020 This manuscript version is made available under the CC-BY-NC-ND 4.0 license
http://creativecommons.org/licenses/by-nc-nd/4.0/

Additional information:

Use policy

The full-text may be used and/or reproduced, and given to third parties in any format or medium, without prior permission or charge, for personal research or study, educational, or not-for-profit purposes provided that:

- a full bibliographic reference is made to the original source
- a link is made to the metadata record in DRO
- the full-text is not changed in any way

The full-text must not be sold in any format or medium without the formal permission of the copyright holders.

Please consult the full DRO policy for further details.

Durham University Library, Stockton Road, Durham DH1 3LY, United Kingdom
Tel : +44 (0)191 334 3042 | Fax : +44 (0)191 334 2971
https://dro.dur.ac.uk

The robust catalysts (Ni_{1-x}-Mo_x/doped ceria and Zn_{1-x}-Mo_x/doped ceria, x = 0.1 and 0.3) for efficient natural gas reforming in solid oxide fuel cells

Amtul Naseer[1], Murid Hussain[2], Imran Shakir[3], Qaisar Abbas[4], Duygu Yilmaz[5], Marriam Zahra[1], Rizwan Raza[1,5*]

[1]Clean Energy Research Lab (CERL), Department of Physics, COMSATS University Islamabad, Lahore Campus, Lahore 54000, Pakistan

[2]Department of Chemical Engineering, COMSATS Institute of Information Technology, Lahore 54000, Pakistan

[3]Department of Materials Science and Engineering, University of California, Los Angeles, CA, 90095, USA

[4]Institute of Engineering and Energy Technologies (IEET), School of Engineering, Computing & Physical Sciences, University of the West of Scotland, Paisley, PA1 2BE, UK

[5]Department of Chemistry and Chemical Engineering, Chalmers University of Technology, S-41296 Göteborg, Sweden

*****Corresponding authors; razahussaini786@gmail.com

HIGH LIGHTS:

- Doping of Mo in Ni-GDC and Zn-GDC anodes for natural gas based SOFC
- Ni-Mo-GDC exhibits maximum power density of 690 $mWcm^{-2}$ at 600 ^oC
- The addition of Mo in Ni-GDC and Zn-GDC anodes improves carbon deposition

Keywords:

Solid Oxide Fuel Cell

Mo doping

Natural gas

Carbon deposition

ABSTRACT

Nickel is a promising catalyst in Solid Oxide fuel cell (SOFC) due to its electrocatalytic performance, however, the practical utilization of Ni-based materials is hindered by the undesirable carbon deposition during methane decomposition. Herein, molybdenum is incorporated into the Ni- and Zn-based cermets (Ni_{1-x}-Mo_x/GDC and Zn_{1-x}-Mo_x/GDC, x = 0.1 and 0.3) to enhance electrocatalytic properties and avoid the carbon deposition during cell operation. The desired composites are synthesized by the impregnation method and adopted as anode in SOFCs. The catalytic activity for methane oxidation has been significantly improved due to the introduction on Mo, which hindered the carbon deposition due to higher graphitization and abundant active sites accessible to fuel. The detailed Raman spectroscopy and conductivity analysis revealed that addition of Mo reduced the amount of deposited carbon and enhanced the electrical conductivity. By using natural gas, as a fuel, the as-prepared Mo-doped Ni-GDC rendered a maximum power density of 690 mW cm^{-2} at 600 ^oC. It is worth mentioning that the achieved stable power density is one of the best in existing literature. The current study presents a novel strategy to improve the catalytic behavior of electrode materials and demonstrate the optimal performance at low operating temperature.

1. Introduction

Solid oxide fuel cell (SOFC) is considered as an efficient electrochemical energy conversion device owing to its high efficiency, fuel flexibility, lower carbon dioxide (CO_2) emission and wide range of operating temperature (500-100 ^oC) [1-2]. In general, hydrogen (H_2) is a preferred fuel for stationary applications due to its high reactivity and stable performance [3-4]. However, current hydrogen production technologies, relying on renewable energy sources, are not mature enough to provide the required amount of hydrogen. Hence, the utilization of currently available hydrocarbons fuels is of utmost significance to meet the current and forecast energy demands. In particular, methane has garnered immense research attention due to its low-cost, abundance and safer storage than the traditional hydrogen fuel [5-11]. Moreover, the direct utilization of hydrocarbons, without external reforming, significantly reduces the operational cost and results in a relatively simple design operation. Owing to the catalytic activity of the fuel exposed electrode, the direct utilization of hydrocarbons in SOFCs is termed as internal reforming (IR), which renders the added advantage of using the electrochemically generated heat [12].

Conventionally, nickel cermet (Ni-YSZ) is used as an anode in hydrogen-based fuel cells due to its excellent catalytic properties for fuel oxidation and high electronic conductivity [13-15]. However, despite the initial improvement, the direct utilization of hydrocarbons renders inferior long-term performance due to carbon deposition on Ni surface, originating from the catalytic decomposition of C-H and C-C bonds and resulting in lesser catalytically active sites [16-17]. Moreover, carbon deposition blocks the porous structure and hinders the gaseous diffusion, altering the anodic structure and resulting in inferior electrochemical performance [18]. Thus, many strategies have been adopted to replace YSZ with novel anode materials, such as gadolinium doped ceria (GDC) and samarium doped ceria (SDC), in SOFCs. Interestingly, doped ceria can be operated at low temperatures due to its mixed ionic and electronic conductivity (MIEC) under reducing atmosphere, resulting in continuous carbon cleaning due to oxygen storage/release and excellent good electrocatalytic activity for methane oxidation [19-21].

Gorte *et al*. [22] investigated rare earth doped ceria, impregnated with CuO, as an anode material for direct utilization of methane in SOFCs. However, the inferior catalytic activity of the studied anode hinders the practical utilization. Kim *et al*. [23] investigated Cu–Ni alloy for direct oxidation of CH_4 and attained a power density of 450 $mWcm^{-2}$ with moderate carbon deposition. Nikolla *et al*. [24] utilized Sn/Ni alloy for direct reforming of different hydrocarbons, such as methane and isooctane, and demonstrated that the carbon deposition could be significantly reduced by incorporating a small amount of Sn and forming Sn/Ni surface alloy. Additionally, the introduction of transition metals into ceria could provide additional pathways for redox reactions at the anode surface, facilitating electrochemical reactions for oxidations of the fuel cell. For instance, Ni-ceria/YSZ anodes exhibited excellent stability during methane reforming and enhanced tolerance to H_2S contaminations [17]. Furthermore, doping of additional metals, such as Mo, Pt and La, to Ni-CeO_2/YSZ anode can enhance the reforming reaction of hydrocarbons.

Huang *et al*. [25-26] studied molybdenum-based perovskite $Sr_2MMoO_{6-\delta}$ (M = Mg, Co, Ni) as SOFC anode material for H_2 and CH_4 fuel. Sr_2CoMoO_6 exhibited a high cell performance in wet H_2 and CH_4, while Sr_2NiMoO_6 exhibited notable power density with methane. Li *et al*. [27, 28] have investigated the oxidation of methanol by using $Sr_2Fe_{1-x}Mo_{1+x}O_6$ and achieved stable performance. Zuhra *et al*. [29] investigated $Ni_{0.5}$ $Zn_{0.5-x}Ce_x$ nanocomposite anodes using methane fuel exhibited maximum power density of 500 $mWcm^{-2}$ at 600 ^oC. The modified anode reduced the carbon deposition hereby enhanced catalytic activity and fuel cell performance. Rizwan *et al*.

[30] studied $Zn_{0.6}Fe_{0.1}Cu_{0.3}$/GDC composite anode for H_2 fuel. Due to lower activation energy, high durability, higher conductivity, composite anode showed maximum power density of 980 $mWcm^{-2}$ at 570 ^oC.

Zn is cheap, non-toxic, and very stable at ambient condition and potential catalysts as methane reformer. The vital role for using GDC and Zn is to increase the catalytic activity as well as to reduce the operating temperature to entirely oxides the dry hydrocarbons fuels directly which may reduce the carbon deposition layer. Moreover, Zn oxide is likely to tune the electronic states of as prepared material which can enhance the catalytic activity of the anode material to improve the overall fuel cell performance. Herein, we aimed to exploit the catalytic effect of Mo and synthesized Mo-doped Ni-GDC and Zn-GDC anodes for natural gas based SOFC to improve the catalytically and redox stability of the methane based SOFC. Moreover, the influence of Mo content on catalytic activity, conductivity and cell performance has been systematically investigated.

2. Experimental

2.1. Material Synthesis

Gadolinium-doped ceria (GDC) powder was prepared using co-precipitation technique [30]. Molybdenum trioxide (MoO_3) and nickel nitrate hexahydrate and zinc nitrate hexahydrate were dissolved separately in 50 ml distilled water. These solutions were mixed vigorously by stirring at 100 ^oC for 1 hour. The molar ratio of Ni (or Zn) to Mo was fixed 0.9:0.1 and 0.7:0.3, which resulted in Sample 1 ($Ni_{0.9}Mo_{0.1}$/GDC), Sample 2 ($Ni_{0.7}Mo_{0.3}$/GDC), Sample 3 ($Zn_{0.9}Mo_{0.1}$/GDC) and Sample 4 ($Zn_{0.7}Mo_{0.3}$/GDC). Then, the obtained solution was impregnated with GDC powder with the weight ratio 1:1 with continuous stirring for 4 hours. Then, water was removed, and as-obtained powder agglomerate was dried in an oven at 120 ^oC for 6 hours. Then, two-step calcination was carried out at 500 ^oC and 700 ^oC for 1 and 2 hours, respectively. Subsequently, the sintered powder was ground in a mortar to form the composite anode. The detailed experimental procedure is schematically illustrated in Figure 1. The well-established lithium transition metal oxide (LiNiCuZn-oxide) LNCZ cathode was synthesized by solid-state reaction method. $Ni_2(NO_3)_3.6H_2O$ (Sigma Aldrich, 99%, USA), $Zn(NO_3)_3.6H_2O$ (Sigma Aldrich, 99%, USA), $Li_2CO_3.3H_2O$ (Sigma Aldrich, 99%, USA) and $Cu(CO_3)_3$ (Sigma Aldrich, 99%, USA), were mixed in a weight ratio of 10:7:2.5:2.5 by using mortar and pestle, followed by calcination at 800 ^oC for 4 hours. The preparation process of GDC electrolyte has been described elsewhere [30].

2.2. Physical Characterization

The XRD patterns of the anode powders were recorded using X-ray Diffractometer (PAN analytical X'Pert Pro MPD, Phillips, Netherlands), equipped with Cu Kα radiations (λ = 1.54 Å), at an applied voltage of 40 kV and current of 30 mA. XRD patterns were collected at a scanning rate 0.01 degree per second in the 2θ range of 10-90 degrees. The average crystallite size was calculated using Debye Scherer's formula, as given below:

$$\mathbf{D = k\,\lambda/\beta Cos\theta} \qquad \mathbf{(1)}$$

Where *D* refers to the crystalline size, *k* is a constant (0.94), λ represents the wavelength of Cu Kα radiations and β denotes the full width at half maximum (FWHM).

The UV-visible spectra were recorded using a double beam Perkin Elmer UV-Visible Diffuse Reflectance Spectroscopic Lambda-35 (UV-35, Perkin Singapore) with the bandwidth of 1 nm at a scan speed of 960 nm/min in the range of 300-1100 nm. The direct band gap was calculated using the Tauc plot (Eq. 2):

$$\mathbf{(\alpha h\nu)^2 = A(h\nu - E_g)^2} \qquad \mathbf{(2)}$$

Where *A* represents the absorption coefficient and *E* refers to the energy of the incident photons.

The cross-section morphology of synthesized nanocomposites was studied by scanning electron microscopy (SEM-Philips XL-30). The surface area (SA), average particle size and pore size distribution were determined by N_2 adsorption/desorption isotherms, recorded at -196 ^oC by using ASAP 2010 porosity analyzer (Micrometrics). For the BET analysis, around 0.5 g of catalyst was used.

In order to study the carbon formation/deposition, Raman spectra of the anode have been collected, before and after exposure to methane (fuel) at 700 ^oC for 1 h , by using InVia Raman microscope (RENISHAW UK), equipped with an excitation laser of 514 nm. Raman spectroscopy is a non-destructive characterization technique, which is extensively used to study the bonding and structural properties of different carbon species. Furthermore, to investigate the electrocatalytic behavior, cyclic voltammetry (CV) was carried out by using the standard three-electrode configuration, where silver chloride (AgCl), platinum (Pt) and modified anode served as reference, counter and working electrodes, respectively, and methane was used as analyte. Nafion solution was taken as electrolyte to enhance conductivity and isopropanol was used as solvent. For CV

measurements, 2 mg of catalysts, 400 ml of isopropanol and 20 ml of nafion solution (5 wt%) were strongly sonicated to get a homogeneous ink. Then, 15 ml of the catalyst ink was deposited on to working electrode. CV curves were recorded by using Gamry framework version 6 at a scan rate of what and in the potential range of 0.50-1.75 mV (vs. Ag/AgCl). The potential was measured between the reference electrode (RE) working electrode (WE), while the current was measured between the counter and working electrodes. The 1M KCl was used as supporting electrolyte and 1M CH_4 was used as fuel and recorded at 500 ^oC. The binary phase diagram of Ni-Mo and Zn-Mo was calculated by CALPHAD *thermocalc software*.

For conductivity measurements, 1 g of composite powder was pressed into pellets by carver hydraulic presser using 3000 KGS force and sintered at 750 ^oC for 2 hours in a muffle furnace. The silver paste was used on both sides of the pellet for current collection. Then, the pellet was placed in a stainless dye for conductivity measurement. The effective area of the pellet was 0.64 cm^2. The DC conductivity was measured using the four-probe method in the temperature range of 300–700 ^oC under H_2 atmosphere. The probe station (Keithley, China), with four tungsten (W) probes, integrated with DC source 2450 (Keithley, Instrument USA), was used for current and voltage measurements. The conductivity was calculated by using Eq. 3:

$$\boldsymbol{\sigma = L/RA} \quad \textbf{(3)}$$

Where L refers to the thickness of the cell, A represents the effective area (0.64 cm^2) and R corresponds to the measured resistance. The conductivity is measured by taking Arrhenius plot of log conductivity verses reciprocal of temperature by Arrhenius Eq.4:

$$\boldsymbol{\sigma = \sigma_o exp(-\frac{E_a}{RT})} \quad \textbf{(4)}$$

Where σ_o is pre-exponential factor, E_a is the activation energy, R is the real gas constant, T is the absolute temperature. The activation energies were calculated from slope of Arrhenius plot by linear fit.

For Fuel cell fabrication, Ni-Mo-GDC, Zn-Mo-GDC powders were uniaxially pressed in 1.5 mm thickness under the pressure of 200 MPa in hydraulic press and used as anode in SOFC having GDC as electrolyte and LNCZ as cathode. Both external sides of each pellet were painted by silver paste to make good electrical contact followed by sintering at 700 ^oC for 1 h. For the performance measurements, methane (70 ml/min) was used as fuel and air (100 ml/min) as oxidant at anode

and cathode sides respectively. I–V/I–P curves were obtained at 600 ^{o}C with computerized instrument (Fuel Cell Electronic load, Model: IT8511, China).

3. Results and Discussion

3.1 Phase Diagram Analysis

The binary phase diagram indicates the composition and phases of Ni-Mo with respect to temperature (*T*). Figure 2a (i) show the phase diagram of bimetallic Ni-Mo catalyst, as reported elsewhere [31-33]. In general, three intermetallic phases, including β phase (Ni_4Mo), γ phase (Ni_3Mo) and δ phase (NiMo), exist at 870 ^{o}C, 910 ^{o}C and 1400 ^{o}C. Pure body-centered cubic Mo melts at 2623°C, whereas pure face-centered cubic Ni melts at 1455 ^{o}C. Figure 2a (i) exhibits that β, δ and γ phases possess tetragonal, orthorhombic and orthorhombic structures, respectively. Moreover, the eutectic phase is formed at 35 % of Mo at 1327 °C. The phase diagram shows that solubility of Ni in Mo at low temperature is extremely low, however, it increased with increasing temperature. Based on these results, we have used mass 3 % Mo, which exhibits the onset of β phase (Ni_4Mo) formation (Figure 2a (ii)). Similarly, Zn-Mo binary phase diagram indicates two intermediate phases of $MoZn_{22}$ (orthorhombic phase) and $MoZn_7$ (Ca7Ge-type cubic) are stable below 463 and 573 ^{o}C [34]. Herein only 3% Mo used does not form any undesirable Zn-Mo phase, as shown in Figure 2(b). These phase diagrams indicate the complete solubility of 3% Mo in Ni and Zn, which is in good agreement with XRD results. Although Fratello *et al*. [32] have reported the formation of $CeNiO_3$ compound near the melting point of NiO (1984 ^{o}C), we have only observed the diffraction peaks of NiO and CeO_2 (Figure 3).

3.2. Crystallite Structure and Microstructure Analysis

Figure 3 shows the XRD patterns of all prepared samples. These results showed that composite oxide material has a multi-phase structure and well-developed crystallinity. The XRD pattern was analyzed by Match software. Figure 3(a) shows that index pattern can be matched with the cubic fluorite structure of ceria (JCPDS #075-0158) and cubic structure of NiO (JCPDS# 073-1523). The characteristics peaks of molybdenum have not been observed in sample 1 due to the low content of Mo. However, when the concentration of Mo was increased from 0.1 to 0.3, additional peaks of (202) and (311), emerged at 2θ = 46.3 and 56.1^{o} corresponding to the orthorhombic structure of MoO. Also, the usual diffraction peaks of NiO and ceria have been observed, as shown in Figure 3(a). Similarly, Figure 3(b) exhibits the diffraction peaks of CeO_2 phase (JCPDS #075-

0158) and hexagonal ZnO phase (JCPDS#36-1451). However, the peak intensity decreased with increasing Mo concentration and slight shifting of ZnO peaks of (100), (013) resulting in decrease in lattice parameter indicates that excessive Mo concentrate on deteriorated the crystallinity of as-prepared powder. One should note that the large difference in ionic radii of Mo^{+6} (0.41 Å), Zn^{+2}(0.60 Å) and Ce^{+3}(1.143 Å) results in lattice mismatch and induces structural stress, which can explain the inferior crystallinity of as-prepared powder with increasing Mo content. Moreover, the calculated crystallite size also decreased, which can be mathematically confirmed by Debye Scherer's equation. With the increase of 2θ value, cosθ increased and resulted in smaller crystallite size. Scherer's equation indicates that FWHM primarily depends on the crystallite size, which implies that a larger FWHM corresponds to the smaller crystallite size. Herein, FWHM increased with increasing Mo concentration from 0.1 to 0.3, resulting in decreased crystallite size. Furthermore, the lattice strain of (111) peak of sample 3 and sample 4 were found to be 0.0021 and 0.0031, respectively, indicating that the lattice strain increased with increasing Mo concentration. It is worth mentioning that the smaller crystallite size is beneficial for obtaining optimal fuel cell performance. The lattice parameters of the as-prepared composite anodes are summarized in Table 1. Figure 3(c) showed the cross-sectional microstructure of best sample $Ni_{0.9}Mo_{0.1}$/GDC anode-supported cell. The average particle size was 11.3 nm. The composite anode shows porous structure for providing high surface area for gas adsorption with more catalytic active sites [35].

Table 1: XRD parameters of $Ni_{0.9}Mo_{0.1}$/GDC, $Ni_{0.7}Mo_{0.3}$/GDC, $Zn_{0.9}Mo_{0.1}$/GDC and $Zn_{0.7}Mo_{0.3}$/GDC composite anodes.

Sample name	Diffraction angle (2θ) (degrees)	FWHM (β) (degree)	Average Crystallite size (D) (nm)	Average atomic distance (d) (Å)	Average lattice constants (Å)	Miller indices (hkl)
$Ni_{0.9}Mo_{0.1}$/GDC	43.51	0.1560	60	2.0783	a= 4.1800	(200)
$Ni_{0.7}Mo_{0.3}$/GDC	43.39	0.260	34	2.0839	a= 4.1684	(200)
$Zn_{0.9}Mo_{0.1}$/GDC	36.36	0.1560	56	2.4633	a= 2.8497	(101)

					c= 4.9358	
$Zn_{0.7}Mo_{0.3}$/GDC	38.36	0.2340	37	2.4945	a= 2.700 c= 4.680	(101)

3.2. BET Surface Area and Porosity Measurements

The BET surface area and porosity results are summarized in Table 2. Combined with crystalline size analysis, it can be concluded that the particle size is inversely related to the surface area. Therefore, sample 2 and sample 4, with smaller crystallite size, resulted in higher specific surface area (SSA) than sample 1 and sample 3 with larger crystallite size. Moreover, the estimated porosity of all samples ranged from 7-12 nm. One should note that $Ni_{0.7}Mo_{0.3}$/GDC exhibited a high specific surface area of 5.5 m^2g^{-1} and SSA dropped from 5.5 to ~3 m^2g^{-1} with the addition of 10 % Mo into NiO-GDC, which is consistent with the available literature [36]. On the other hand, $Zn_{0.9}Mo_{0.1}$/GDC anode exhibited a specific surface area of 1.98 m^2g^{-1}. Similar to the smaller crystallite size, the higher specific surface area translates into higher conductivity and optimal fuel cell performance by increasing the number of active catalytic sites, as shown by our results in the subsequent section.

Table 2: BET surface area and porosity of as-prepared composite anodes.

Samples	Sample 1 ($Ni_{0.9}Mo_{0.1}$/GDC)	Sample 2 ($Ni_{0.7}Mo_{0.3}$/GDC)	Sample 3 ($Zn_{0.9}Mo_{0.1}$/GDC)	Sample 4 ($Zn_{0.7}Mo_{0.3}$/GDC)
Porosity	9	12	7	8.5
Surface	3.2952	5.5569	1.9883	2.1108

3.3. UV-visible Analysis

UV-visible analysis was used to study the optical properties of the as-prepared anode powder, in general, and band gap of bimetallic catalyst, in particular. Figure 4 shows Tauc plots of $(\alpha hv)^2$as a function of photon energy (hv) for $Ni_{0.9}Mo_{0.1}$/GDC, $Ni_{0.7}Mo_{0.3}$/GDC, $Zn_{0.7}Mo_{0.3}$/GDC and $Zn_{0.7}Mo_{0.3}$/GDC powder with different Mo concentrations. Figure 4(a) shows that the sample with the lowest conductivity and surface area, i.e., Ni:Mo (0.9:0.1), exhibited the highest band gap of 3.7 eV whereas the sample with higher conductivity, i.e., Ni:Mo (0.7:0.3), rendered smaller band

gap of 3.1 eV (Figure 4b). Similarly, the band gap of Mo-doped Zn-GDC decreased from 3.7 to 2.9 eV with increasing Mo concentration from 0.1 to 0.3, as shown in Figure 4(c-d). Mo-doped Zn-GDC sample show lower bandgap as compared to Ni-doped Zn-GDC exhibiting semiconductor behavior. The results reveal that the composite materials with a lower bandgap possess higher conductivity, which can lead to superior fuel cell performance. These results are also consistent with XRD results.

3.4. Raman Analysis

One should note that the carbon deposition on the electrode surface renders the detrimental effect on SOFC performance and stability by covering the porous surface, making it electrochemically inactive during FC operation. Herein, Raman spectroscopy has been employed to investigate the carbon deposition during SOFC operation. Figure 5(a-b) shows the Raman spectra of $Ni_{0.9}Mo_{0.1}$/GDC and $Ni_{0.7}Mo_{0.3}$/GDC electrode before and after methane (CH_4) exposure at 700 ^oC for 1 h. Prior to fuel cell operation, the Raman spectrum consists of several bands of NiO (>400 cm^{-1}). The first four bands, located at 437 cm^{-1}, (730-881 cm^{-1}) and (986-1200 cm^{-1}), correspond to the IP,(2P) 2TO, (2P) TO+LO vibrational modes of nickel oxide.

Moreover, the absence of 1P mode in sample 2 confirmed the excellent crystallinity of $Ni_{0.7}Mo_{0.3}$/GDC electrode. The Raman peak at 1170 cm^{-1} represents a combined influence of different modes of ceria, such as F_{2g}, A_{1g} and E_g. After methane exposure, Raman spectra of composite anode exhibited two broad peaks (centered at 1300-1348 cm^{-1} and 1580-1593 cm^{-1}), corresponding to D and G bands of carbon, respectively. One should note that the D band indicates the disorder in deposited carbon and G band corresponds to the stretching of carbon bonds. Moreover, *R* represents the degree of graphitization of the deposited carbon, where higher *R*-value refers to the lower degree of graphitization.

R value can be obtained from the intensity ratio of D and G bands as below in Eq.5.

$$\mathbf{R} = \frac{\mathbf{I_D}}{\mathbf{I_G}} \qquad \mathbf{(5)}$$

The deposited carbon on the surface of Ni-Mo/GDC anode exhibited an R-value of 1.3 and 1.167 rendered carbon deposition by increasing molybdenum concentration.

Figure 5 (c-d) shows the Raman spectra of $Zn_{0.9}Mo_{0.1}$/GDC and $Zn_{0.7}Mo_{0.3}$/GDC anodes before and after methane exposure. The Raman spectra of as-prepared Mo-doped Zn-GDC anodes exhibit

a sharp and maximum intensity mode at 456 cm^{-1}, corresponding to F_{2g} symmetric breathing mode of the oxygen (O^{-2}) atoms around cerium cations. However, in the range of 500-600 cm^{-1}, relatively lower intensity peaks represent the oxygen vacancies within the ceria lattice due to extrinsic cation doping, i.e., samarium [37]. The Raman peaks at 330 cm^{-1}, 900 $cm^{-1}$and 1150 cm^{-1} of ZnO lattice correspond to multi-phonon process. Similar to the Mo-doped Ni-GDC, the Raman peak at 1170 cm^{-1} emerged due to the mixing of different modes of ceria, such as F_{2g}, A_{1g} and E_g. When Mo concentration was increased from 0.1 to 0.3 ($Zn_{0.7}Mo_{0.3}$/GDC), F_{2g} mode has been shifted to lower wavenumber, exhibiting a red shift and coupling of electronic molecular vibrational modes due to the presence of excessive Mo in ceria lattice. After natural gas exposure, the Raman spectra of Mo-doped Zn-GDC exhibited two additional bands at 1350 $cm^{-1}$and 1490 cm^{-1}, corresponding to D and G bands of deposited carbon. Moreover, the G band shifted to a higher wavenumber with increasing Mo concentration, indicating the occurrence of double bonds between carbon atoms, which resonate at higher energy. Furthermore, the R-value of fuel-exposed $Zn_{0.9}Mo_{0.1}$/GDC and $Zn_{0.7}Mo_{0.3}$/GDC anodes was found to be 1.03 and 1.06, respectively. The higher R-value of $Zn_{0.7}Mo_{0.3}$/GDC exhibited lower graphitization degree with increasing Mo concentration.

3.5. Electrochemical Analysis

Figure 6(a) shows CV curves of the as-prepared catalyst, measured at different scan rates, ranging from 20 to 100 mVs^{-1} at 500 ^{o}C. CV curves were used to understand the oxidation behavior of methane (CH_4). Moreover, the Randles-Sevcik equation [38] was used to analyze the diffusion coefficient for CH_4, as given below:

$$\mathbf{I_p = 2.69 \times 10^5\ ACD_O^{\frac{1}{2}} v^{\frac{1}{2}}} \quad \textbf{(6)}$$

Where I_p refers to the peak current (A), n denotes the number of transferred electrons, C corresponds to the concentration of analyte (mol cm^{-3}), v represents the scan rate (V s^{-1}), A refers to the electrode area (cm^2) and D_o represents the diffusion coefficient. Diffusion coefficient represents the diffusion of analyte, such as methane, through the electrolyte, resulting in the efficient transfer of electrons. Diffusion coefficient can be calculated by taking the slope of peak current versus the square root of scan rate, as shown in Figure 6(b). The estimated diffusion coefficient is 3.078 x 10^{-5} cm^{-2} s^{-1}. The higher diffusion coefficient of methane provides greater availability of active areas at electrode for adsorbed species to oxidize into carbon dioxide.

Moreover, the maximum current has been achieved at 100 mV s^{-1}. Herein, the best sample was selected to assess the electrocatalytic activity based on the diffusion coefficient. Bimetallic $Ni_{0.7}Mo_{0.3}$/GDC catalyst exhibited maximum surface area and highest conductivity, enhancing the facile electron transfer process and resulting in optimal electrocatalytic activity for methane oxidation. The oxidation peak height has corresponding values as 1.7 and 0.67 mA cm^{-2}.

3.6. Electrical Conductivity

The conductivity analysis was performed to evaluate the effect of temperature on the performance of the as-prepared composite anodes, areas, by using four-probe methods. Figure 7 shows the Arrhenius plot of conductivity versus temperature (K^{-1}), exhibiting that the conductivity increased with increasing temperature which obeys Arrhenius equation. The activation energy calculated from slope of Arhenius plot of composite anodes by linear fitting were 0.234 eV, 0.59 eV, 0.78 eV and 0.0265 eV depicted in inset of Figure 7(a-d). The activation energy plays important role to estimate perforamnce for oxygen ion conductivity in anode/cathode material. The results revealed that $Ni_{0.7}Mo_{0.3}$/GDC electrode, with highest specific surface area, exhibited superior electrical conductivity of 1.4 S cm^{-1}, which is ~111 times higher than the electrical conductivity of $Ni_{0.9}Mo_{0.1}$/GDC electrode (0.0126 S cm^{-1}). The lower value of activation energy of 0.234 eV emphasized high catalytic activity of $Ni_{0.7}Mo_{0.3}$/GDC. Figure 7 (c-d) shows that the electrical conductivity of Mo-doped Zn-GDC samples increased. Both sample 4 ($Zn_{0.7}Mo_{0.3}$/GDC) and sample 3 ($Zn_{0.9}Mo_{0.1}$/GDC) rendered the maximum electrical conductivity of 0.27 S cm^{-1} and 0.00153 S cm^{-1}.

These results confirm that the incorporation of Mo into Ni-GDC and Zn-GDC anodes significantly enhanced the electrical conductivity, which is conducive to efficient electronic and ionic transfer and superior fuel cell performance.

3.7. Fuel Cell Performance

The electrochemical performance of the as-prepared fuel cells (pellets) was evaluated under a methane environment. Methane, as a fuel with 70ml/min and air with 100ml/min, as an oxidant, were supplied to the anode and cathode side, respectively. Methane is internally reformed by Ni-Mo catalyst into hydrogen (H_2) and carbon (C). Carbon and hydrogen are further oxidized to form carbon dioxide and water along with the release of two electrons at 600 ^oC. The possible reactions during internal reforming, at the anode electrode, are given below (Eqs. 7-10):

$$CH_4 \rightarrow C + 2H_2 \quad (7)$$

$$C + O^{2-} \rightarrow CO \quad (8)$$

$$CO + O^2 \rightarrow CO_2 \quad (9)$$

$$H_2 + O^2 \rightarrow H_2O + 2e^- \quad (10)$$

Figure 8 shows the I-V and I-P curves of Ni-Mo/GDC|GDC|LNCZ and Zn-Mo/GDC|GDC|LNCZ cells. Sample 1, 2, 3 and 4 delivered an excellent power density of 500, 690, 300 and 600 mW cm^{-2} at 600 ^oC, respectively. It is noteworthy that the obtained power densities are exceptionally higher than the previously reported data with similar cell configurations. For instance, Escudero *et al.* [39] have carried out methane oxidation at Mo-Ni ceria anode and reported a much lower power density of ~350 mW cm^{-2} at a significantly higher operating temperature of 850 ^oC. Moreover, Li *et al*. [40] have utilized methanol, as a fuel, and achieved a maximum power density of 680 mW cm^{-2} with Ni-SDC anode at 700 ^oC, whereas we have attained a power density of 690 mW cm^{-2} at a much lower operating temperature (600 ^oC) by using natural gas as a fuel. Furthermore, the as-fabricated cells have been tested for 50 hrs, rendering stable output power and OCVs. The stability has been studied at 600 ^oC for conductivity, open circuit voltage and under current load. The prepared material shows very stable conductivity, and overall fuel cell stable open circuit voltage. Further the same fuel cell shows the stable performance under constant current load. The results have been shown in supplementary figures S1, S2 and S3.

The increment in OCV (0.91-1.01 V) and power density of Mo-doped Ni- and Zn-GDC anodes can be credited to the hindered carbon deposition during oxidation process as methane decomposition process, as depicted in Figure 8. The utilization of Mo-doped Zn-GDC anode delivered optimal electrochemical performance due to better catalytic properties of Mo doped samples (Figure 8). One should note that the maximum power density of 690 mW cm^{-2} has been demonstrated by sample 2 ($Ni_{0.7}Mo_{0.3}$/GDC) at a low operating temperature of 600 ^oC. These results confirm that the incorporation of Mo into Ni- and Zn-GDC cermets is an efficient strategy to improve the overall performance of SOFCs.

3.8. Reaction Mechanism Using FactSage-Equilibrium Module

FactSage 7.2 software was used for simulating the reaction mechanisms of the samples. The calculations were performed for 600 °C under the presumption of an isothermal and standard state

with the use of Pure Substance (FactPS)-Oxide (FToxid) databases. The equilibrium calculations were based on the Gibbs energy minimization method. In this method, elements or compounds react or partially react to reach a state of chemical equilibrium. To calculate the multicomponent equilibrium compositions, amounts and properties of raw materials were given and the chemical reaction characteristics included phases and species were specified. Calculated gaseous species within the amount of less than 0.001 mol were neglected to simplify the results. Following to that, FactSage-Reaction Module was used to calculate the enthalpy of the reactions. Calculations were carried out based on the assumption of using 1 mole of fuel.

Table 3: Thermodynamic calculations to study the reaction mechansim when methane was used as fuel

Sample	ΔH°_{25} **(kJ/mole)**	ΔG°_{25} **(kJ/mole)**	ΔH°_{600} **(kJ/mole)**	ΔG°_{600} **(kJ/mole)**
$Mo_{0.1}Ni_{0.9}GDC^{\#}$	126	68	128.5	-46
$Mo_{0.3}Ni_{0.7}GDC$	161.6	88	163.6	-57
$Mo_{0.1}Zn_{0.9}GDC^{\#}$	90.83	58	100.27	-12.5
$Mo_{0.3}Zn_{0.7}GDC^{\#}$	123	72	129	-31.4

#Carbon deposition

In these calculations, it has been observed that the theoretical carbon deposition was the least for sample 4 and the highest for the sample 3 but not in sample 2 (In equilibrium calculations).

- Therefore the main mechanism for Mo/Ni systems:

$MoO_3+NiO+CeO_2 \rightarrow MoC^*+Ni+C^{**}+aCH_4^{***}+bH_2+cH_2O+dCO$ (a,b,c,d depends on the system)

*If the amount of methane changes, MoO_2 and Mo_2C can form as well. But a mole of CH_4 ends up with MoC for this temperature

**Depending on the carbon deposition. This does not occur for sample 2

***Depending on the carbon deposition or amount of methane

- The reaction mechanism for Mo/Zn systems:

$MoO_3+NiO+CeO_2 \rightarrow MoC+C+aCH_4+bH_2+cH_2O+dCO$ (a,b,c,d depends on the system)

4. Conclusions

In summary, molybdenum-based composites, Ni_{1-x}-Mo_x/GDC and Zn_{1-x}-Mo_x/GDC (x = 0.1 and 0.3), have been successfully synthesized by using impregnation method and adopted as anode materials for solid oxide fuel cells (SOFCs), using methane (natural gas) as a fuel. XRD analysis revealed that composite oxide anode has a multi-phase structure and well-developed crystallinity. Moreover, the addition of 0.01% Mo resulted in an increase in specific surface area (SSA) and Ni_{1-x}-Mo_x/GDC (x = 0.1 and 0.3) resulted in SSA values of 5.5 and 3 $m^2 g^{-1}$, respectively, which is consistent with the available literature. The improved fuel cell performance can be ascribed to the increased SSA, which rendered abundant active sites.

The Mo-doped composite rendered improved catalytic activity for methane oxidation. The cell, with sample 2 ($Ni_{0.7}Mo_{0.3}$/GDC) as an anode, attained a maximum OCV of 1.01 V and a power density of 690 $mWcm^{-2}$ by using domestic natural gas at 600 ^oC. One should note that the obtained power density is highest among the published literature with similar cell configuration and operating temperatures. Even with Mo-doped Zn-GDC anode, the cell performance has been significantly improved. Meanwhile, the incorporation of Mo suppressed the carbon deposition at the electrode surface and resulted in enhanced stability and fuel cell performance.

It is expected from the present work that Ni-Mo based potential anode materials shall be explored for a wide array of applications, such as energy conversion, storage and catalysis. After compositional and microstructural optimization, the anode-supported SOFC configuration is recommended to obtain optimal performance.

Acknowledgment

Higher Education commission of Pakistan

References

[1] Zhu, B., Fan, L., & Lund, P. (2013). Breakthrough fuel cell technology using ceria-based multi-functional nanocomposites. *Applied energy*, *106*, 163-175.

[2] McIntosh, S., & Gorte, R. J. (2004). Direct hydrocarbon solid oxide fuel cells. *Chemical reviews*, *104*(10), 4845-4866.

[3] Cimenti, M., & Hill, J. M. (2010). Importance of pyrolysis and catalytic decomposition for the direct utilization of methanol in solid oxide fuel cells. *Journal of Power Sources*, *195*(1), 54-61.

[4] Lototskyy, M. V., Tolj, I., Pickering, L., Sita, C., Barbir, F., & Yartys, V. (2017). The use of metal hydrides in fuel cell applications. *Progress in Natural Science: Materials International*, *27*(1), 3-20.

[5] Murray, E. P., Tsai, T., & Barnett, S. A. (1999). A direct-methane fuel cell with a ceria-based anode. *Nature*, *400*(6745), 649-651.

[6] Park, S., Vohs, J. M., & Gorte, R. J. (2000). Direct oxidation of hydrocarbons in a solid-oxide fuel cell. *Nature*, *404*(6775), 265-267.

[7] Cimenti, M., & Hill, J. M. (2010). Direct utilization of methanol and ethanol in solid oxide fuel cells using Cu–Co (Ru)/Zr0. 35Ce0. 65O2− δ anodes. *Journal of Power Sources*, 195(13), 3996-4001.

[8] Su, C., Ran, R., Wang, W., & Shao, Z. (2011). Coke formation and performance of an intermediate-temperature solid oxide fuel cell operating on dimethyl ether fuel. *Journal of Power Sources*, 196(4), 1967-1974.

[9] Hua, B., Yan, N., Li, M., Sun, Y. F., Zhang, Y. Q., Li, J., ... & Luo, J. L. (2016). Anode-Engineered Protonic Ceramic Fuel Cell with Excellent Performance and Fuel Compatibility. *Advanced Materials*, 28(40), 8922-8926.

[10] Sengodan, S., Choi, S., Jun, A., Shin, T. H., Ju, Y. W., Jeong, H. Y., ... & Kim, G. (2015). Layered oxygen-deficient double perovskite as an efficient and stable anode for direct hydrocarbon solid oxide fuel cells. *Nature Materials*, 14(2), 205.

[11] Wang, W., Wang, F., Chen, Y., Qu, J., Tadé, M. O., & Shao, Z. (2015). Ceramic lithium ion conductor to solve the anode coking problem of practical solid oxide fuel cells. *ChemSusChem*, 8(17), 2978-2986.

[12] Niakolas, D. K. (2014). Sulfur poisoning of Ni-based anodes for solid oxide fuel cells in H/C-based fuels. *Applied Catalysis A: General*, *486*, 123-142.

[13] Yang, C., Li, W., Zhang, S., Bi, L., Peng, R., Chen, C., & Liu, W. (2009). Fabrication and characterization of an anode-supported hollow fiber SOFC. *Journal of Power Sources*, *187*(1), 90-92.

[14] Bengaard, H. S., Nørskov, J. K., Sehested, J., Clausen, B. S., Nielsen, L. P., Molenbroek, A. M., & Rostrup-Nielsen, J. R. (2002). Steam reforming and graphite formation on Ni catalysts. *Journal of Catalysis*, 209(2), 365-384.

[15] Baker, R. T. K., Barber, M. A., Harris, P. S., Feates, F. S., & Waite, R. J. (1972). Nucleation and growth of carbon deposits from the nickel catalyzed decomposition of acetylene. *Journal of catalysis*, 26(1), 51-62.

[16] Steele, B. C. (1999). Fuel-cell technology: running on natural gas. *Nature*, *400*(6745), 619.

[17] Kong, J., Sun, K., Zhou, D., Zhang, N., Mu, J., & Qiao, J. (2007). Ni–YSZ gradient anodes for anode-supported SOFCs. *Journal of Power Sources*, *166*(2), 337-342.

[18] Boder, M., & Dittmeyer, R. (2006). Catalytic modification of conventional SOFC anodes with a view to reducing their activity for direct internal reforming of natural gas. *Journal of Power Sources*, *155*(1), 13-22.

[19] Wang, J. B., Jang, J. C., & Huang, T. J. (2003). Study of Ni-samaria-doped ceria anode for direct oxidation of methane in solid oxide fuel cells. *Journal of power sources*, *122*(2), 122-131.

[20] Li, P., Yu, B., Li, J., Yao, X., Zhao, Y., & Li, Y. (2016). Improved activity and stability of Ni-Ce0. 8Sm0. 2O1. 9 anode for solid oxide fuel cells fed with methanol through addition of molybdenum. *Journal of Power Sources*, 320, 251-256.

[21] Tian, D., Liu, W., Chen, Y., Yu, W., Yu, L., & Lin, B. (2015). A robust NiO–Sm0. 2Ce0. 8O1. 9 anode for direct-methane solid oxide fuel cell. *Materials Research Bulletin*, *71*, 1-6.

[22] McIntosh, S., Vohs, J. M., & Gorte, R. J. (2003). Role of hydrocarbon deposits in the enhanced performance of direct-oxidation SOFCs. *Journal of the Electrochemical Society*, 150(4), A470-A476.

[23] Kim, H., Lu, C., Worrell, W. L., Vohs, J. M., & Gorte, R. J. (2002). Cu-Ni cermet anodes for direct oxidation of methane in solid-oxide fuel cells. *Journal of the Electrochemical Society*, *149*(3), A247-A250.

[24] Nikolla, E., Schwank, J., & Linic, S. (2009). Direct electrochemical oxidation of hydrocarbon fuels on SOFCs: improved carbon tolerance of Ni alloy anodes. *Journal of the Electrochemical Society*, *156*(11), B1312-B1316.

[25] Huang, Y. H., Dass, R. I., Xing, Z. L., & Goodenough, J. B. (2006). Double perovskites as anode materials for solid-oxide fuel cells. *Science*, *312*(5771), 254-257.

[26] Huang, Y. H., Liang, G., Croft, M., Lehtimaki, M., Karppinen, M., & Goodenough, J. B. (2009). Double-perovskite anode materials Sr2MMoO6 (M= Co, Ni) for solid oxide fuel cells. *Chemistry of Materials*, *21*(11), 2319-2326.

[27] Wang, Z., Tian, Y., & Li, Y. (2011). Direct CH4 fuel cell using Sr2FeMoO6 as an anode material. *Journal of Power Sources*, *196*(15), 6104-6109.

[28] Li, H., Tian, Y., Wang, Z., Qie, F., & Li, Y. (2012). An all perovskite direct methanol solid oxide fuel cell with high resistance to carbon formation at the anode. *Rsc Advances*, *2*(9), 3857-3863.

[29] Tayyab, Z., Rehman, S. U., Shakir, I., Khan, M. A., Mushtaq, N., Alvi, F., ... & Raza, R. (2020). Catalytic study of efficient nanocomposites {Ni0. 5 Zn0. 5− x Cex-oxides electrodes} for natural gas-fed fuel cells. *Materials Research Express*, *7*(1), 015508.

[30] Raza, R., Zhu, B., & Fransson, T. H. (2011). Zn0. 6Fe0. 1Cu0. 3/GDC Composite Anode for Solid Oxide Fuel Cell. *Journal of Fuel Cell Science and Technology*, *8*(3).

[31] Arya, A., Banerjee, S., Das, G. P., Dasgupta, I. N. D. R. A., Saha-Dasgupta, T., & Mookerjee, A. (2001). A first-principles thermodynamic approach to ordering in Ni-Mo alloys. *Acta materialia*, *49*(17), 3575-3587.

[32] Fratello, V. J., Berkstresser, G. W., Brandle, C. D., & Graitis, A. V. (1996). Nickel containing perovskites. *Journal of crystal growth*, *166*(1-4), 878-882.

[33] Casselton, R. E. W., & Hume-Rothery, W. (1964). The equilibrium diagram of the system molybdenum-nickel. *Journal of the Less Common Metals*, 7(3), 212-221.

[34] Raghavan, V. (2009). Al-Mo-Zn (Aluminum-Molybdenum-Zinc). *Journal of phase equilibria and diffusion*, *30*(6), 630.

[35] Zhang, Y., Zha, S., & Liu, M. (2005). Dual-Scale Porous Electrodes for Solid Oxide Fuel Cells from Polymer Foams. *Advanced Materials*, *17*(4), 487-491.

[36] Wang, X., Zhang, J., Zhang, X., & Zhu, Y. (2017). Characterization, uniformity and photo-catalytic properties of graphene/TiO 2 nanocomposites via Raman mapping. *Optics Express*, *25*(18), 21496-21508

[37] Maher, R. C., Duboviks, V., Offer, G. J., Kishimoto, M., Brandon, N. P., & Cohen, L. F. (2013). Raman spectroscopy of solid oxide fuel cells: technique overview and application to carbon deposition analysis. *Fuel Cells*, 13(4), 455-469.

[38] Janjua, N. K., Jabeen, M., Islam, M., Yaqub, A., Sabahat, S., Mehmood, S., ... & Abbas, G. (2015). Electrochemical Properties of Barium Cerate Doped with Zinc for Methanol Oxidation. *Journal of the Chemical Society of Pakistan*, 37(5).

[39] Escudero, M. J., de Parada, I. G., Fuerte, A., & Serrano, J. L. (2014). Analysis of the electrochemical performance of MoNi–CeO2 cermet as anode material for solid oxide fuel cell. Part I. H2, CH4 and H2/CH4 mixtures as fuels. *Journal of Power Sources*, *253*, 64-73.

[40] Li, P., Yu, B., Li, J., Yao, X., Zhao, Y., & Li, Y. (2016). Improved activity and stability of Ni-Ce0. 8Sm0. 2O1. 9 anode for solid oxide fuel cells fed with methanol through addition of molybdenum. *Journal of Power Sources*, *320*, 251-256.

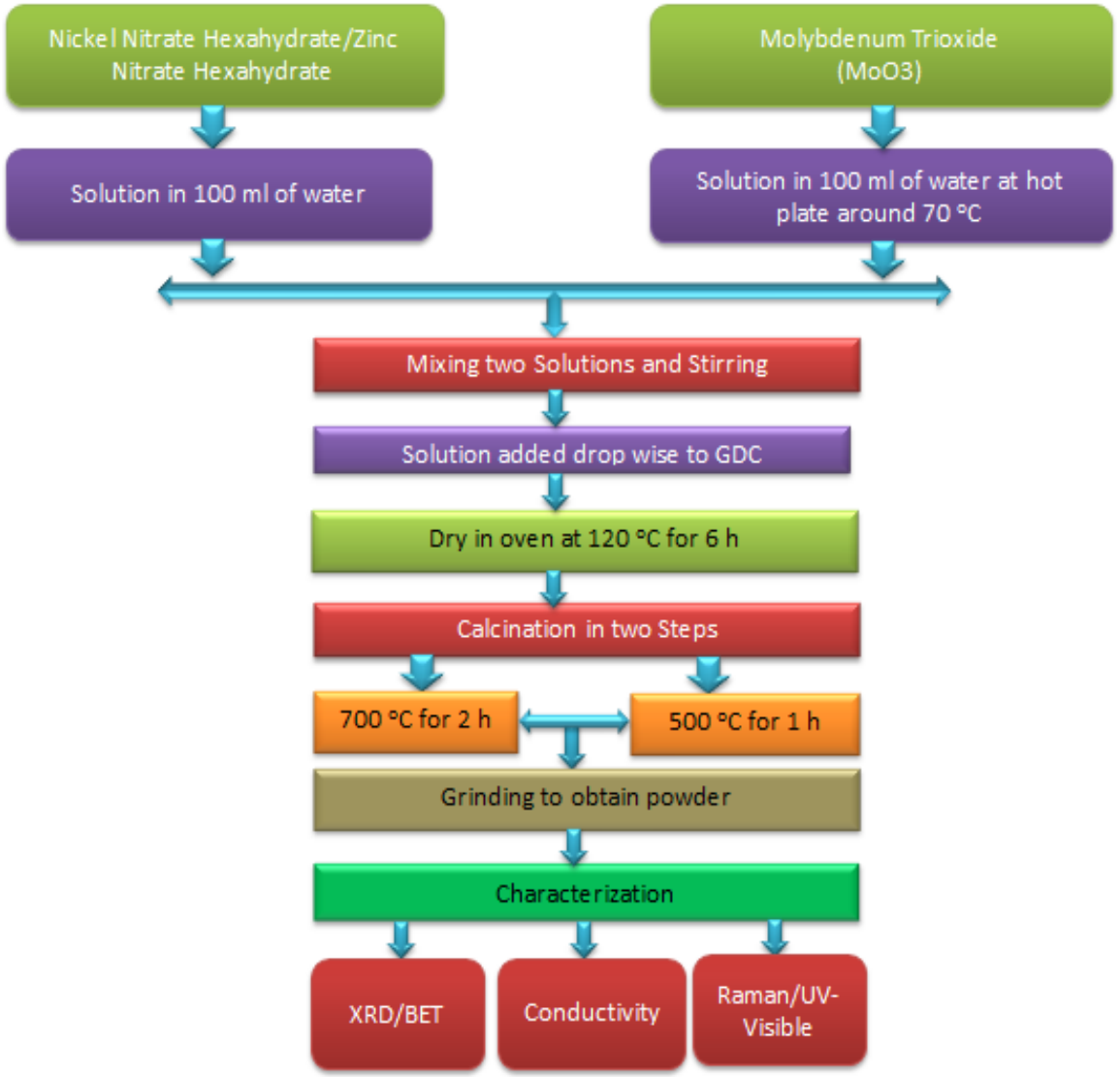

Figure 1: Flow chart of the synthesis procedure of composite anodes

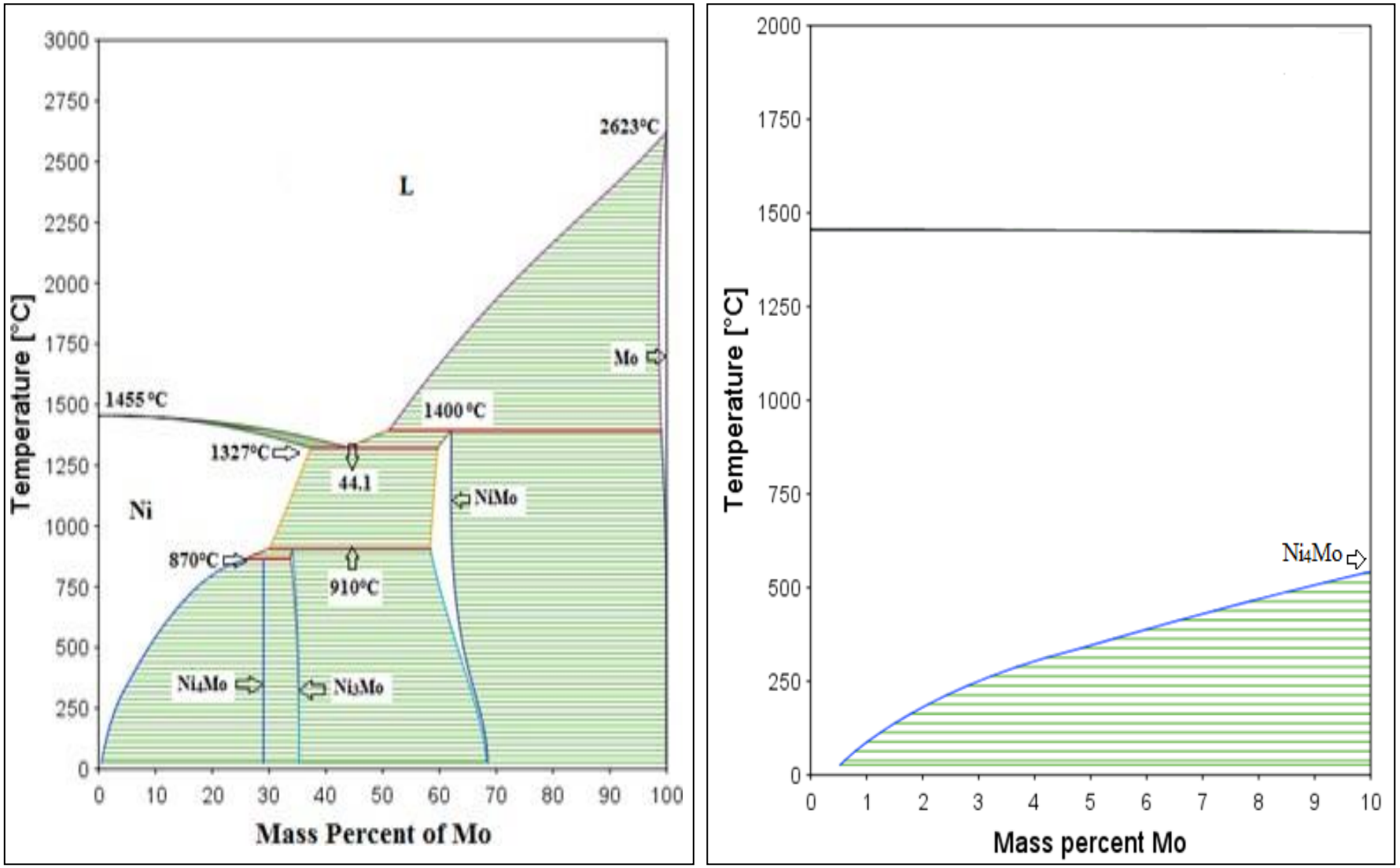

Figure 2 (a): Binary phase diagram of (i) Ni-Mo [Ref. 32] and (ii) zoom-in region of 0-10% Mo.

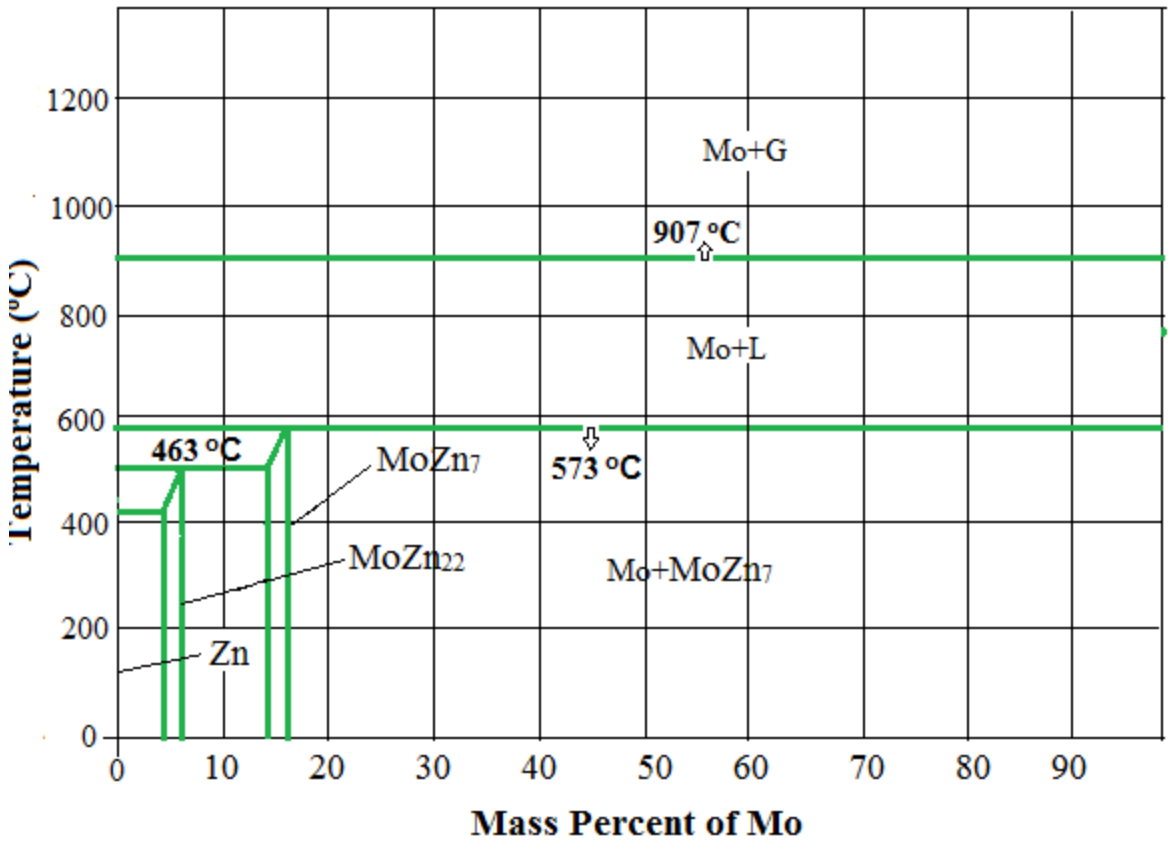

Figure 2(b): Binary phase diagram of Zn-Mo, as calculated by Thermocalc software.

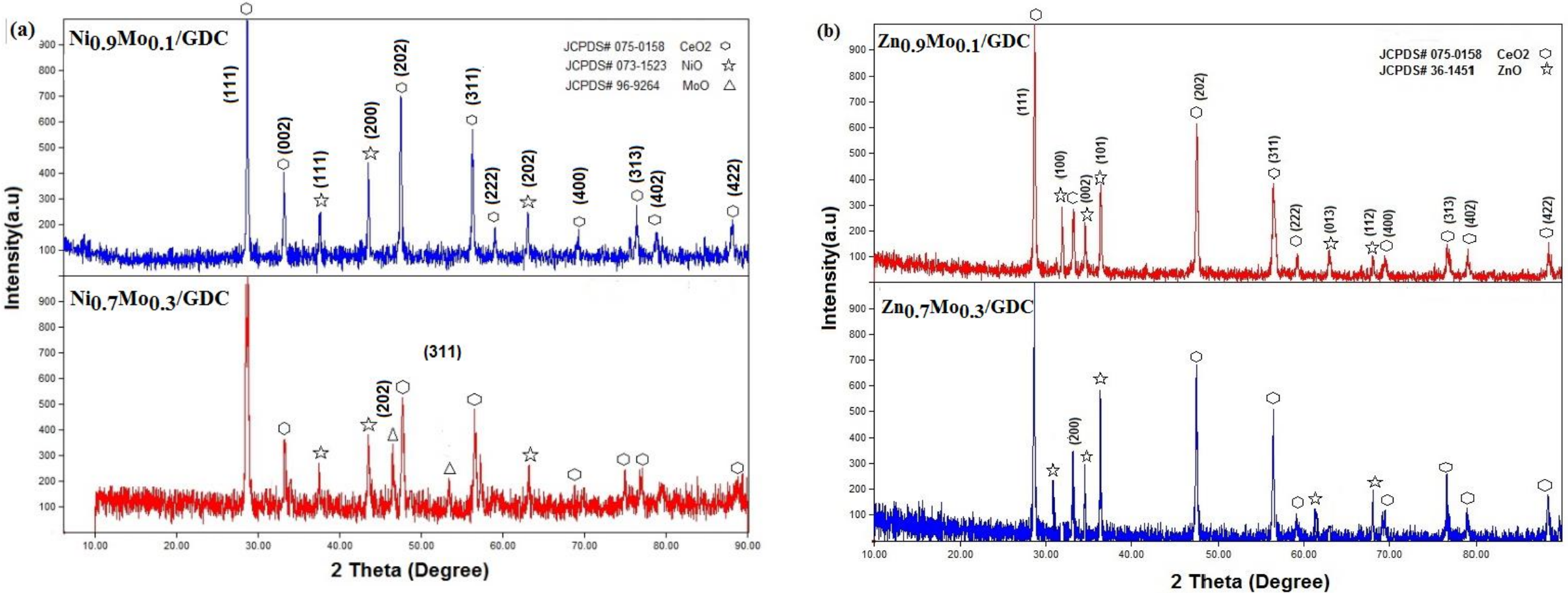

Figure 3 (a,b): XRD patterns of as-prepared composite anodes: (a) $Ni_{0.9}Mo_{0.1}$/GDC, $Ni_{0.7}Mo_{0.3}$/GDC (b) $Zn_{0.9}Mo_{0.1}$/GDC and $Zn_{0.7}Mo_{0.3}$/GDC

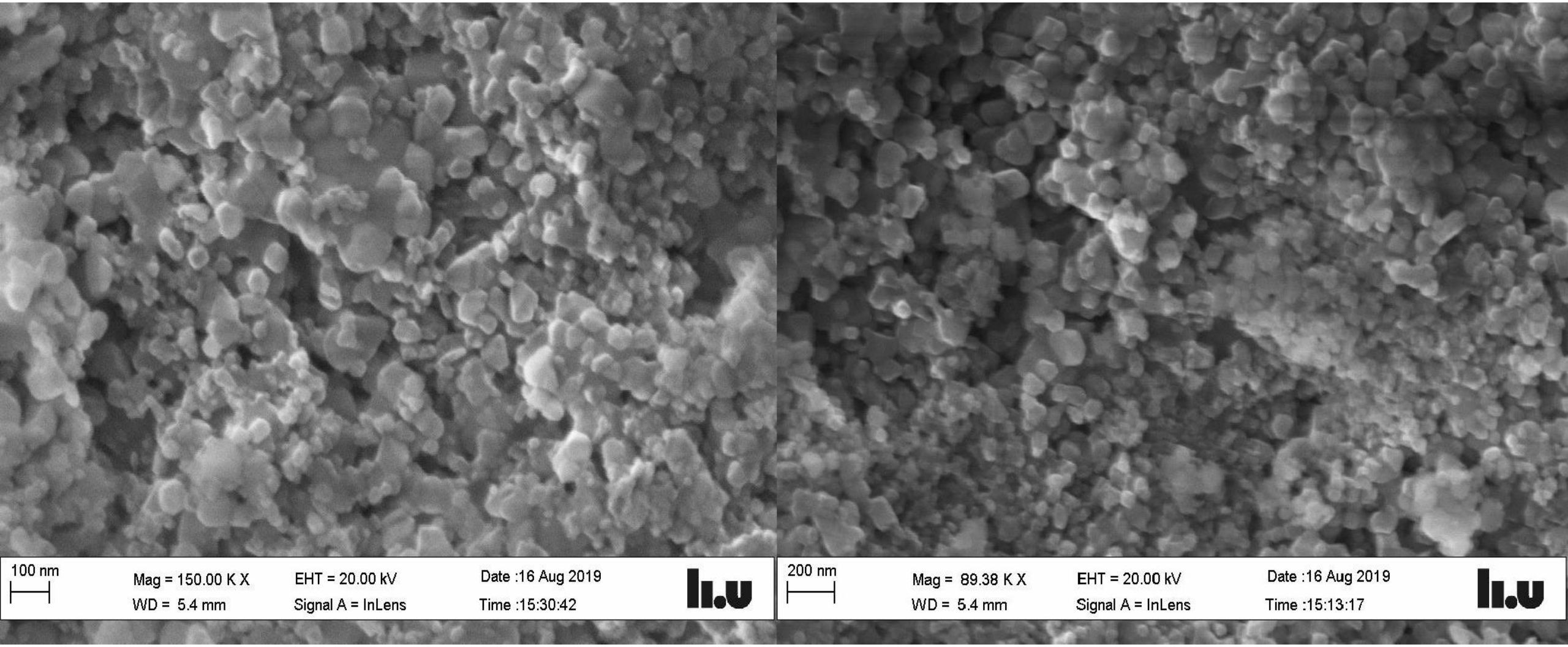

Figure 3 (c): Microstructure analysis of best sample 1 $Ni_{0.9}Mo_{0.1}$/GDC.

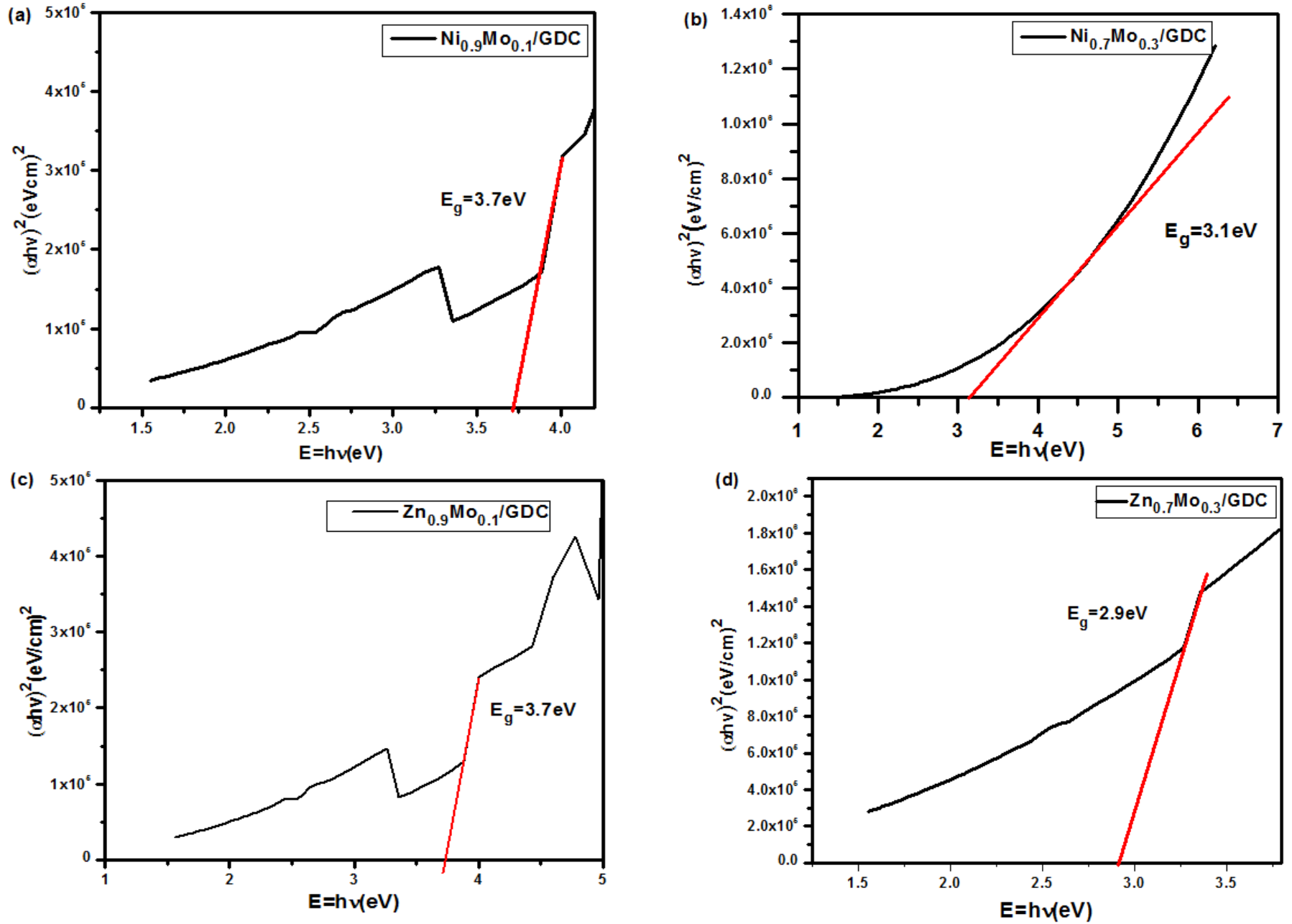

Figure 4 (a,b,c,d): Tauc plots of $(\alpha h\nu)^2$ *vs.* photon energy (hν) of the as-prepared composite anodes

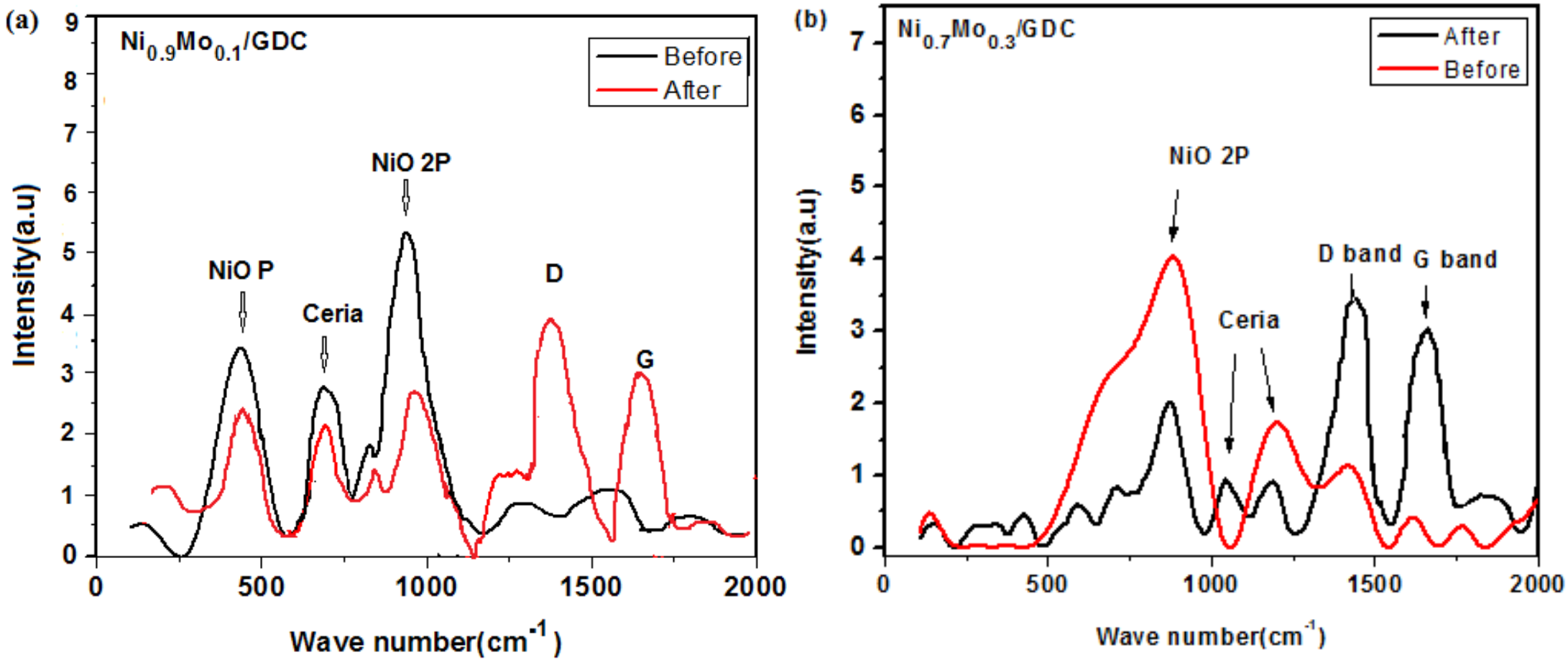

Figure 5 (a, b): Raman Spectra of $Ni_{0.9}Mo_{0.1}$/GDC and $Ni_{0.7}Mo_{0.3}$/GDC before and after methane exposure.

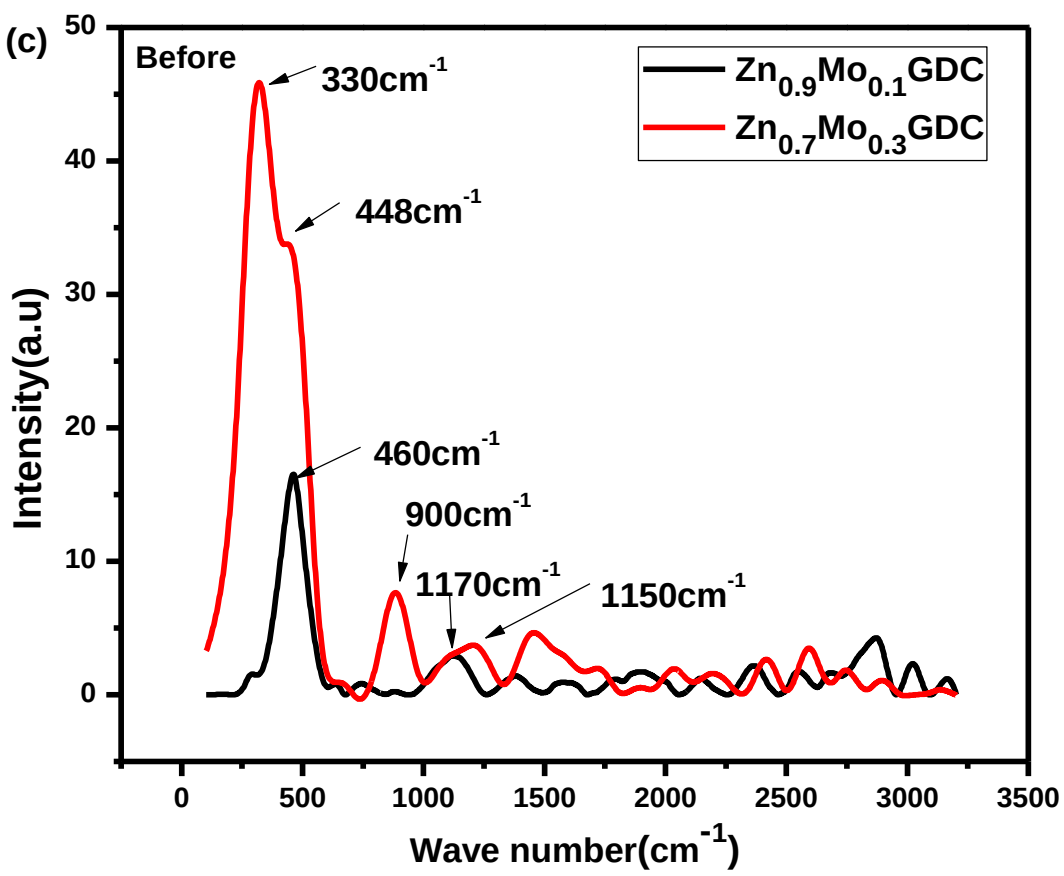

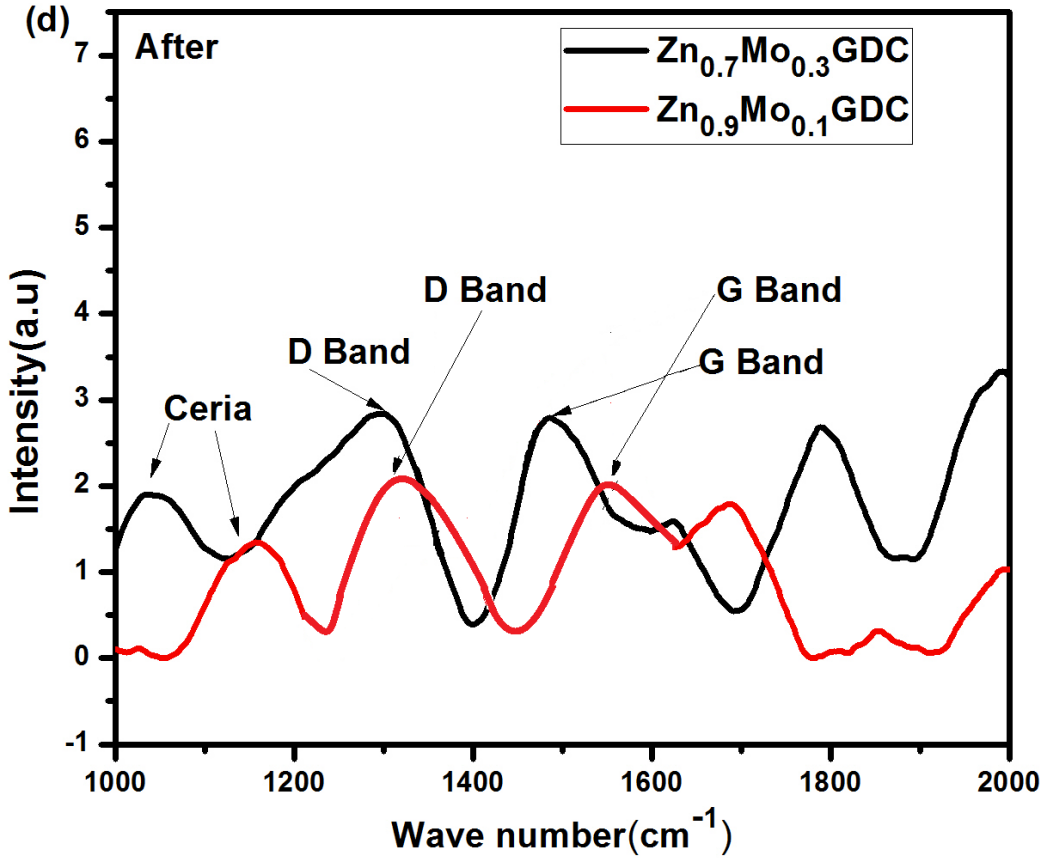

Figure 5(c,d): Raman Spectra of $Zn_{0.9}Mo_{0.1}$/GDC and $Zn_{0.7}Mo_{0.3}$/GDC before and after methane exposure.

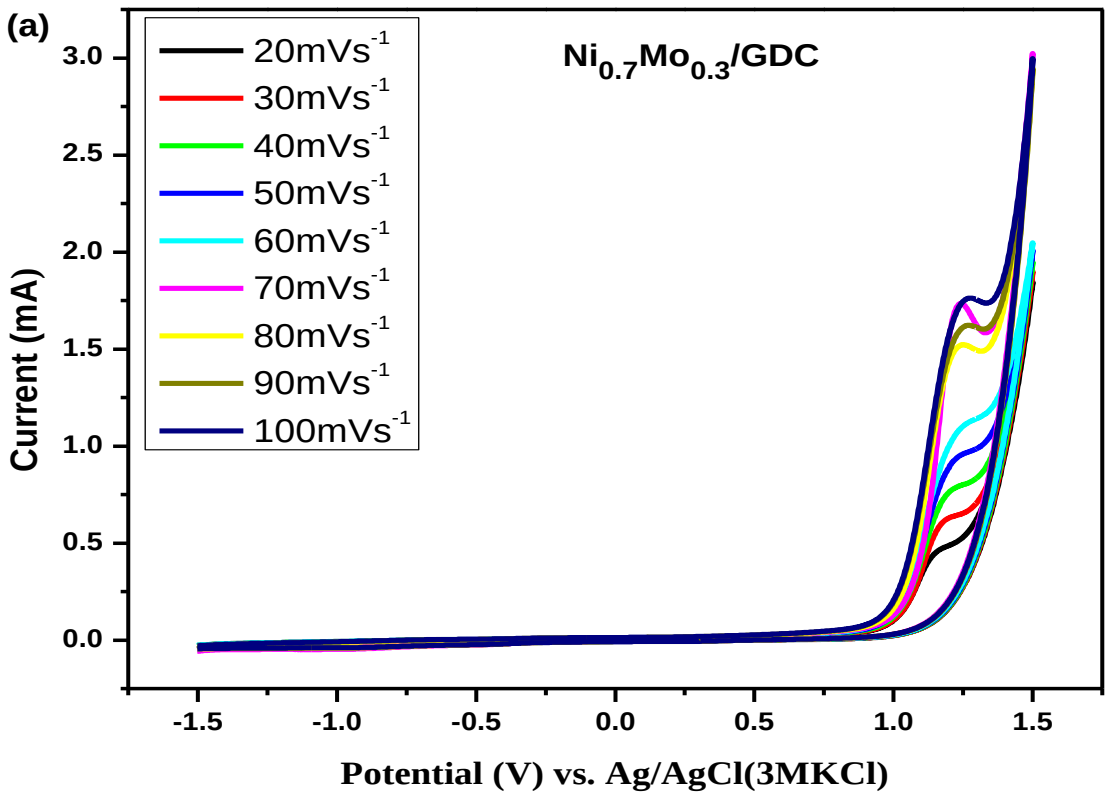

Figure 6: (a) CV curves of $Ni_{0.7}Mo_{0.3}$/GDC electrode, measured at different scan rates (20-100 mV s^{-1}) by using methane gas

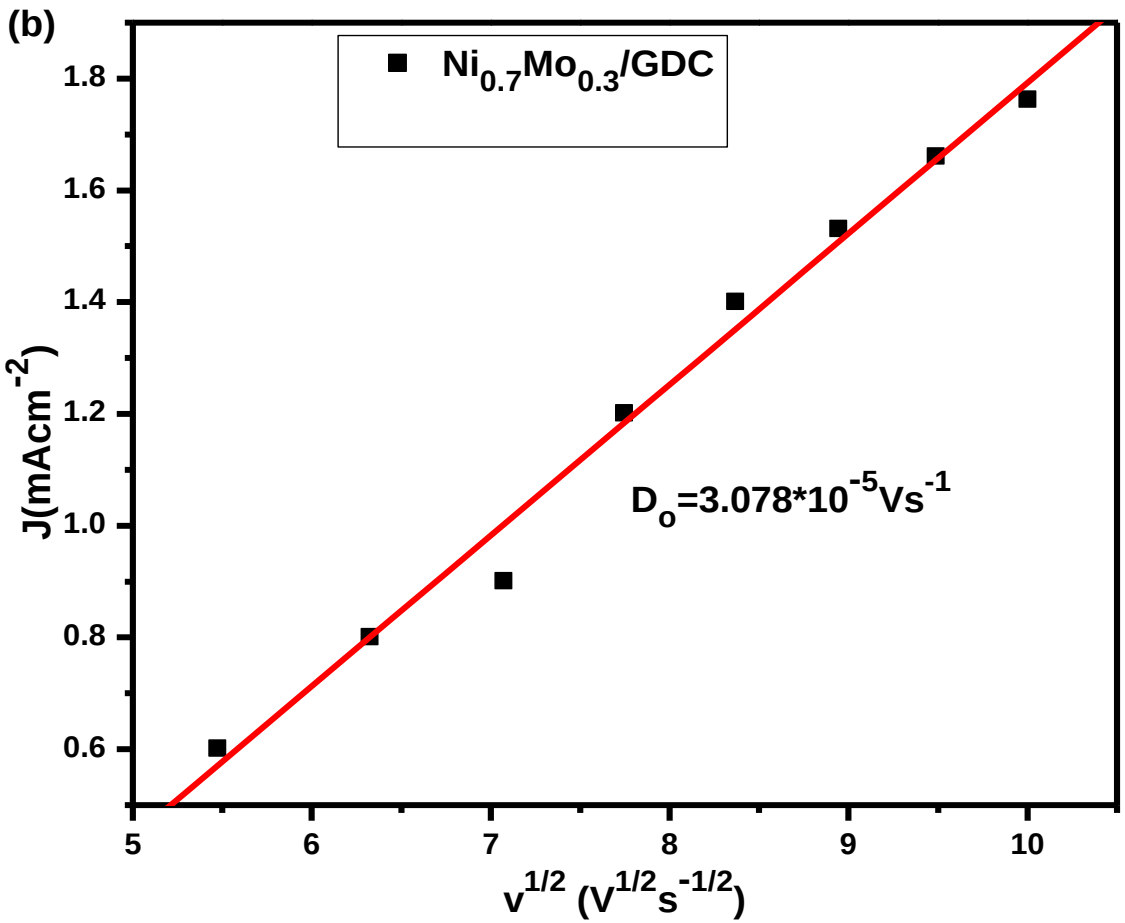

Figure 6: (b) Current density versus square root of scan rate to estimate the diffusion coefficient.

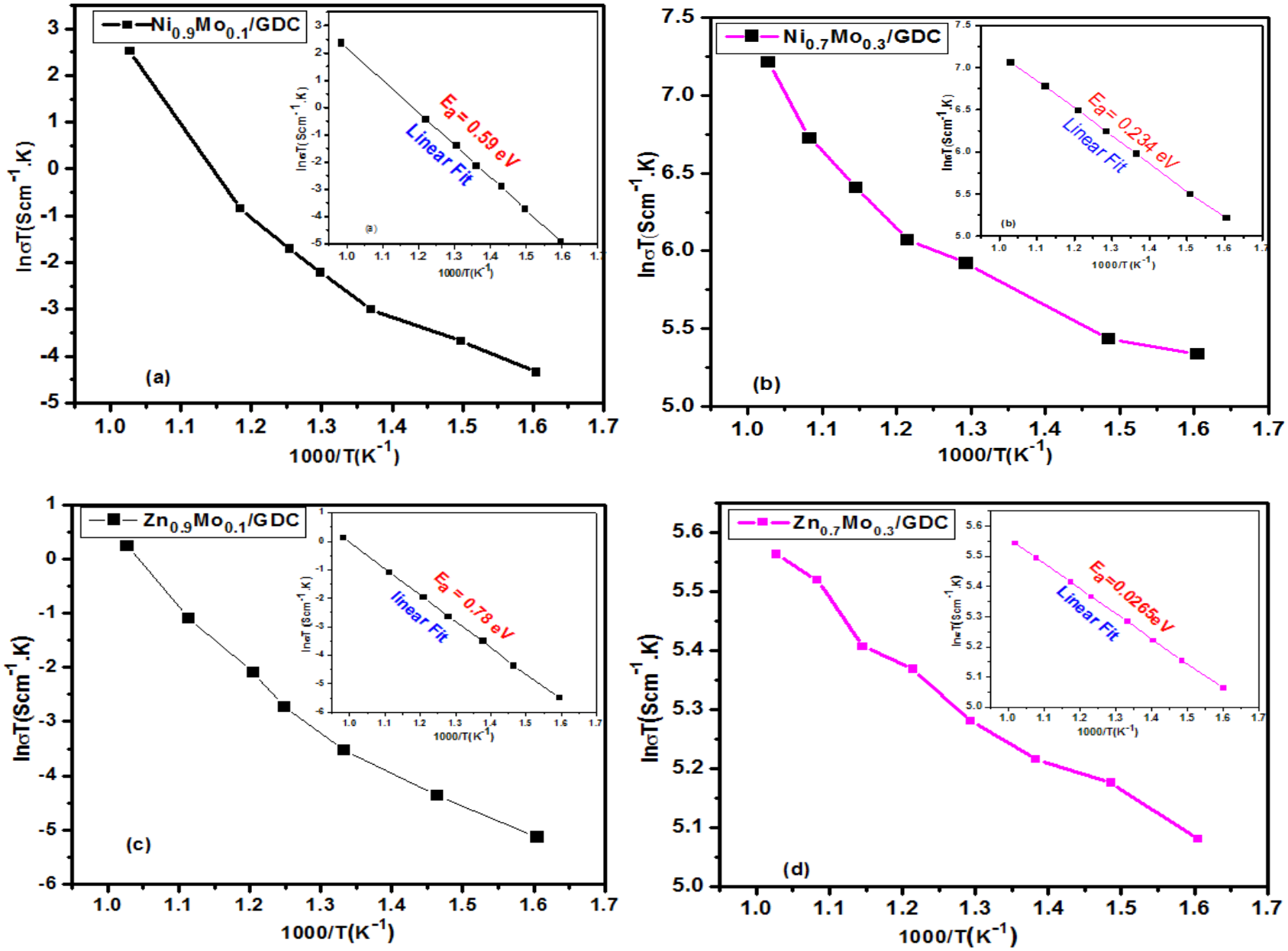

Figure 7: Arrhenius plots of the as-prepared composite anodes in H_2 atmosphere: (a) $Ni_{0.9}Mo_{0.1}$/GDC, (b) $Ni_{0.7}Mo_{0.3}$/GDC, (c) $Zn_{0.9}Mo_{0.1}$/GDC and (d) $Zn_{0.7}Mo_{0.3}$/GDC.

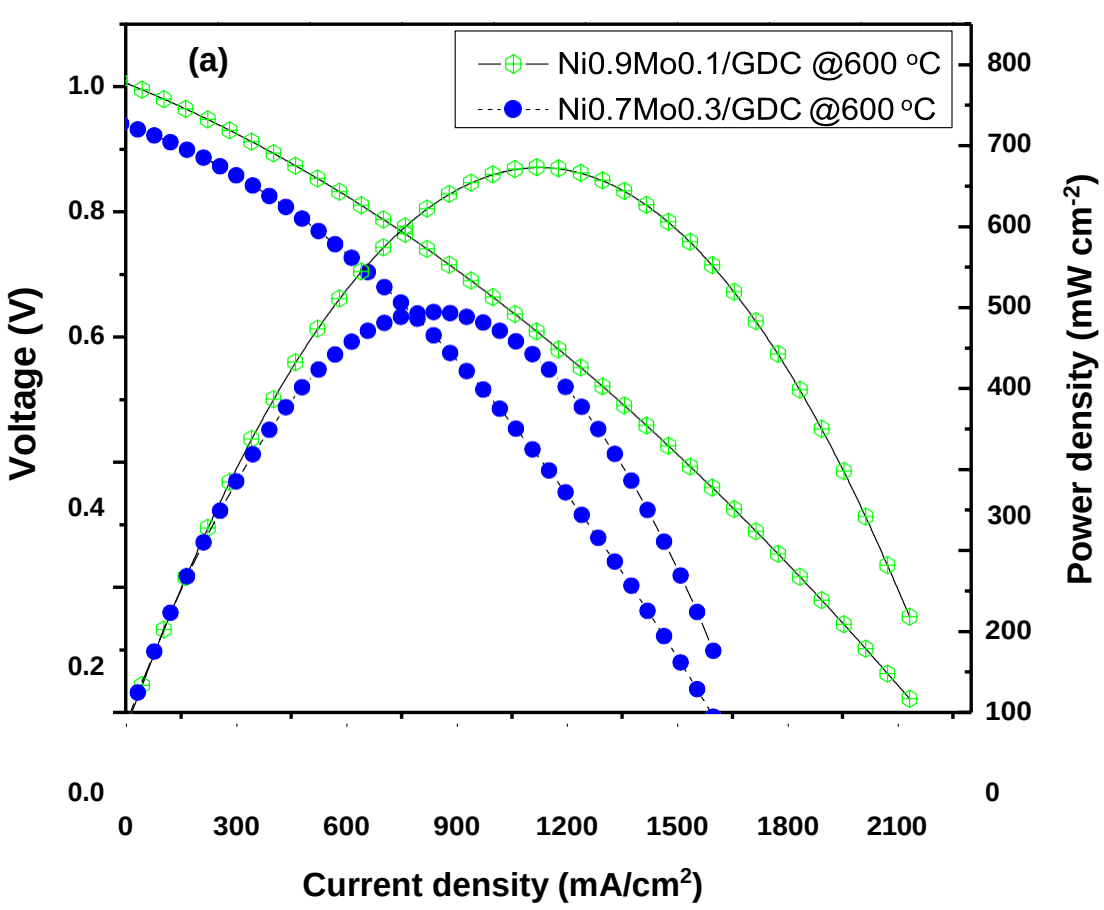

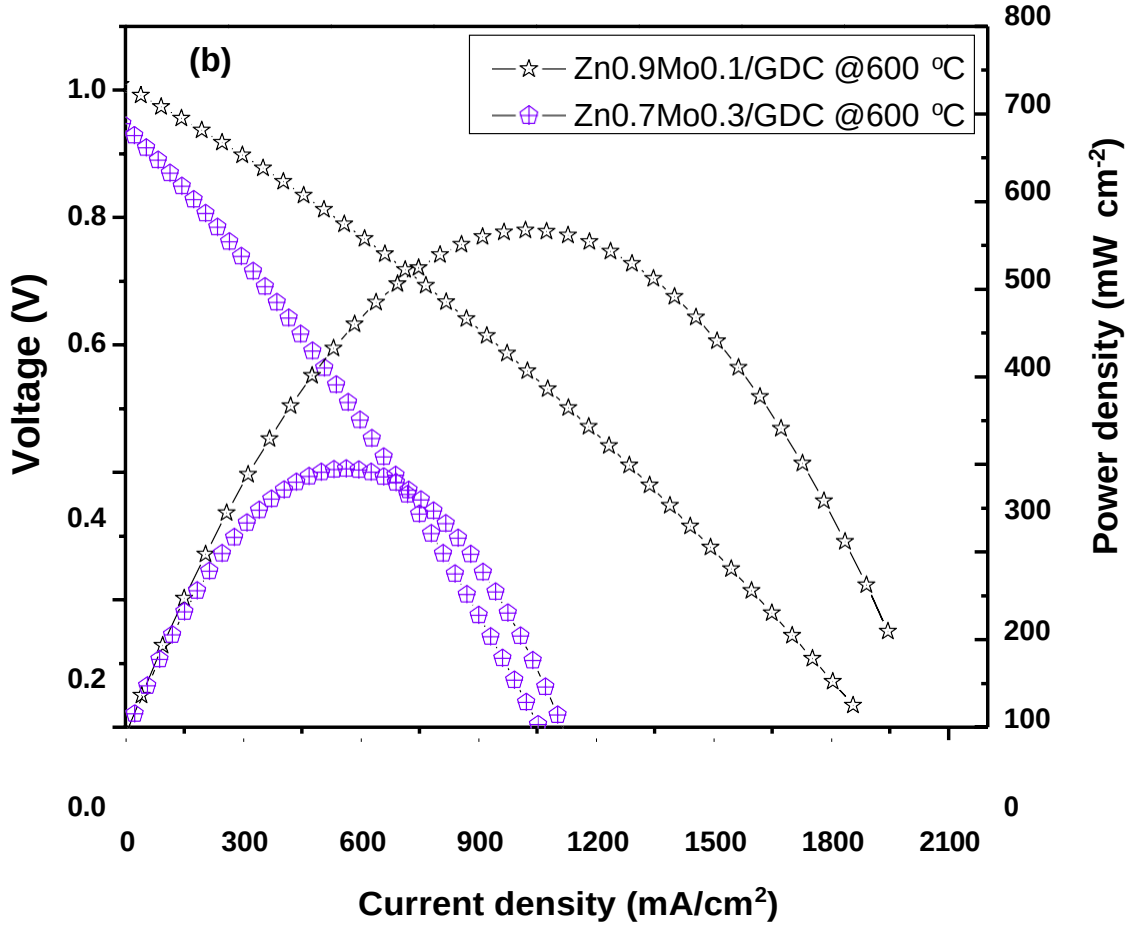

Figure 8: Electrochemical performance of as-prepared cells:

(a) I-V and I-P curves of $Ni_{0.9}Mo_{0.1}$/GDC and $Ni_{0.7}Mo_{0.3}$/GDC anode materials, and

(b) I-V and I-P curves of $Zn_{0.9}Mo_{0.1}$/GDC and $Zn_{0.7}Mo_{0.3}$/GDC anode materials